A General Approach to Sampled-Data Modeling for Ripple-Based Control—Part II: Constant ON-Time and Constant OFF-Time Control

Na Yan, Xinbo Ruan, *Fellow, IEEE*, and Xin Li, *Member, IEEE*

***Abstract*—This part is the second part of this article and mainly presents the sampled-data modeling method for the dc–dc converters with the constant ON-time (COT) and constant OFF-time (COFT) controls. Compared with the constant frequency control in the first part, the duty cycle perturbation signal in the COT/COFT control is found to have two sets of narrow pulse signals in each switching period. Then, by establishing the relationship between the two sets of signals and using Shannon's sampling theorem, the transfer functions of the modulator and the loop gain are derived. Based on the theoretical results, the phenomenon that a current-mode constant ON/OFF time controlled buck converter is stable at any duty cycle, and the instability of a voltage-mode constant ON/OFF-time controlled buck converter with the smaller time constant of the output capacitor could be predicted. Moreover, the sampled-data modeling method is further extended to the digital control by taking a digitally current-mode controlled buck converter as an example. Simulation results are provided to confirm the validity of the proposed modeling method.**

***Index Terms*—Constant ON-time (COT), modulator, sampled-data modeling, sideband effect, variable frequency control.**

I. Introduction

CONSTANT ON-time (COT) control and constant OFF-time (COFT) control are two variable frequency control schemes in the ripple-base control for ease of design and the fast transient response [1]-[5]. As an important application scenario, the buck converter with the COT control has been widely used in microprocessor power supply design due to the improvement of light-load efficiency by reducing the switching frequency [1].

However, what comes along with the advantages is the complexity when modeling the converters with the COT and COFT controls. Since the small ripple hypothesis is no longer satisfied, the widely used averaging technique becomes less effective in this case.

Manuscript received February 18, 2021; revised July 7, 2021 and October 17, 2021; accepted November 20, 2021. Date of publication December 6, 2021; date of current version February 18, 2022. This work was supported by the National Science Foundation of China for Distinguished Young Scholars under Grant 51525701. Recommended for publication by Associate Editor L. Corradini. *(Corresponding author: Xinbo Ruan.)*

Na Yan and Xinbo Ruan are with the Center for More-Electric-Aircraft Power System, College of Automation Engineering, Nanjing University of Aeronautics and Astronautics, Nanjing 211106, China (e-mail: yanna@nuaa.edu.cn; ruanxb@nuaa.edu.cn).

Xin Li is with the School of Electrical and Electronic Engineering, Nanyang Technological University, Singapore 639798 (e-mail: li-xin@ntu.edu.sg).

Color versions of one or more figures in this article are available at https://doi.org/10.1109/TPEL.2021.3132624.

Digital Object Identifier 10.1109/TPEL.2021.3132624

In [6], the describing function (DF) method is presented for the buck converter with the ripple-based control, where the power stage and the modulator are treated as a single entity. The core principle of the DF method is to perform Fourier transform on the time domain expression of the inductor current or output voltage signal, which requires complex mathematical derivation. Although it is stated in [6] that the DF method is an approximate procedure for analyzing nonlinear control problems, neither the derivation process nor the obtained results, shows how the nonlinear modulator affects the dynamic performance of the converter.

In [7] and [8], the modeling for voltage-mode ripple-based controlled buck converter is studied, where the output voltage is divided into three parts: the inductor current signal scaled by the equivalent series resistor (ESR) of the output capacitor (represented by R_c), the load current signal scaled by R_c, and the voltage v_c across the output capacitor (excluding the voltage across R_c). Then, by neglecting the switching ripple of v_c, it is stated in [7] and [8] that the method proposed for current-mode constant ON-time (C-COT) control and current-mode constant OFF-time (C-COFT) control in [6] can be directly applied to voltage-mode constant ON-time (V-COT) control and voltage-mode constant OFF-time (V-COFT) control. However, the assumption that R_c is much larger than the capacitive reactance of the output capacitor makes the prediction results not that general.

In [9], the transfer function of the modulator is derived by using the DF technique for the C-COT and C-COFT controls. However, the value of the feedback signal, is regarded as a constant at the moment when the switch is turned ON (in the C-COFT control) or turned OFF (in the C-COT control) in the perturbed state (see (2) and (3) in [9]), which is not true in general.

In Part I of this article, it is indicated that the modulators in all various ripple-based control schemes can be understood as a sampler from the perspective of small-signal analysis, and the sampled-data modeling method is proposed to derive the transfer function of the modulator for constant frequency control. In this part, the method proposed in Part I will continue to be used to model the modulator for the C-COT and C-COFT controls.

The rest of this article is organized as follows. Section II presents the proposed sampled-data modeling method for a C-COT/C-COFT controlled buck converter, and the obtained theoretical results are then used to analyze the converter stability and verified by simulation. By using the same methodology,

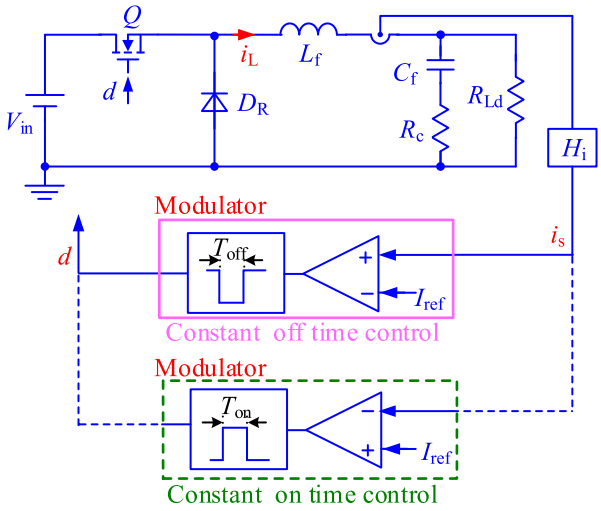

Fig. 1. C-COT/C-COFT controlled buck converter. The power stage and the modulator are connected by the solid lines under C-COT and the dashed lines under C-COFT.

the small-signal models of a V-COT/V-COFT controlled buck converter are given in Section III followed up with the stability analysis and simulation verifications. Section IV discusses the unification of the modeling methods for average control and ripple-based control. Section V extends the proposed method to the digital control, and a digitally current-mode controlled buck converter is taken as an example to introduce the modeling process. Finally, Section VI concludes this article.

II. Sampled-Data Modeling for C-COT/C-COFT

In this section, the sampled-data modeling for C-COT and C-COFT is presented first, and the obtained theoretical models are used to analyze the converter stability followed up with simulation verifications.

A. Sampled-Data Modeling

Fig. 1 shows a buck converter under the C-COT or C-COFT control, where $V_{\rm in}$ is the input voltage, L_f is the filter inductor, C_f is the output capacitor, R_c is the ESR of the output capacitor, and $R_{\rm Ld}$ is the load resistor, i_L is the inductor current and i_s is its feedback signal, d is the duty cycle signal, H_i is the inductor current sense gain, $T_{\rm on}$ and $T_{\rm off}$ are the ON-time (C-COT) and OFF-time (C-COFT) of the switch in each switching period, respectively. Denoting $T_{\rm s}$ as the switching period in steady state, and the corresponding switching (angular) frequency is represented by $f_{\rm s}(\omega_{\rm s})$. Moreover, the part from $i_{\rm s}$ to d is referred to as the modulator.

For C-COT, the switch Q turns ON once $i_{\rm s}$ drops below the reference $I_{\rm ref}$. After conducting for a fixed time $T_{\rm on}$, Q turns OFF, and remains in OFF-state until $i_{\rm s}$ drops below $I_{\rm ref}$ again. For C-COFT, the switch Q turns OFF once $i_{\rm s}$ rises above $I_{\rm ref}$. After a fixed-time $T_{\rm off}$, Q turns ON and remains in ON-state until $i_{\rm s}$ reaches $I_{\rm ref}$ again.

Figs. 2 and 3 illustrate the operating principles of the modulator under the C-COT control and C-COFT control, respectively,

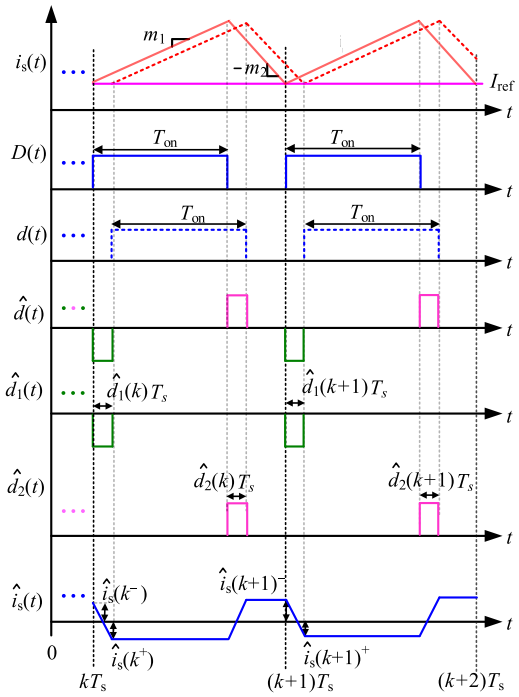

Fig. 2. Key waveforms of the modulator under C-COT in the perturbated state.

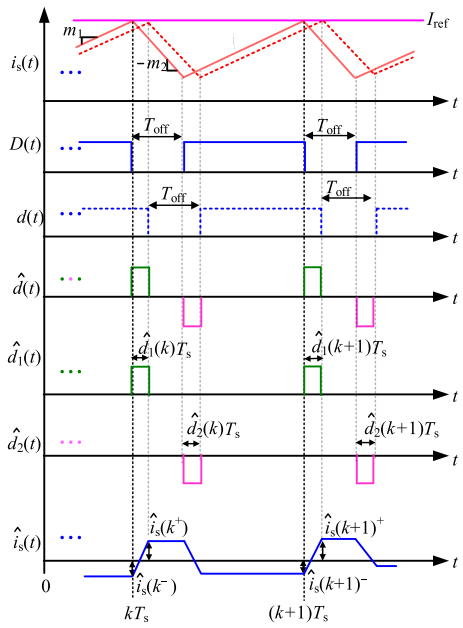

Fig. 3. Key waveforms of the modulator under C-COFT in the perturbated state.

where the upper solid and dotted lines represent $i_{\rm s}$ at steady state and perturbed state, respectively, $D(t)$ and $d(t)$ are the duty cycle signal at steady state and perturbed state, respectively. $\hat{i}_{\rm s}$ and $\hat{d}$ denote the perturbation signal in $i_{\rm s}$ and d, respectively. Besides, m_1 and $-m_2$ are the slopes of $i_{\rm s}$ during the ON-time and OFF-time of the switch, respectively.

As seen from Figs. 2 and 3, $\hat{d}$ can be divided into two series of signals, the one represented by $\hat{d}_1$ is a series of narrow pulse signals at each sampling instant, i.e., the intersection instant of

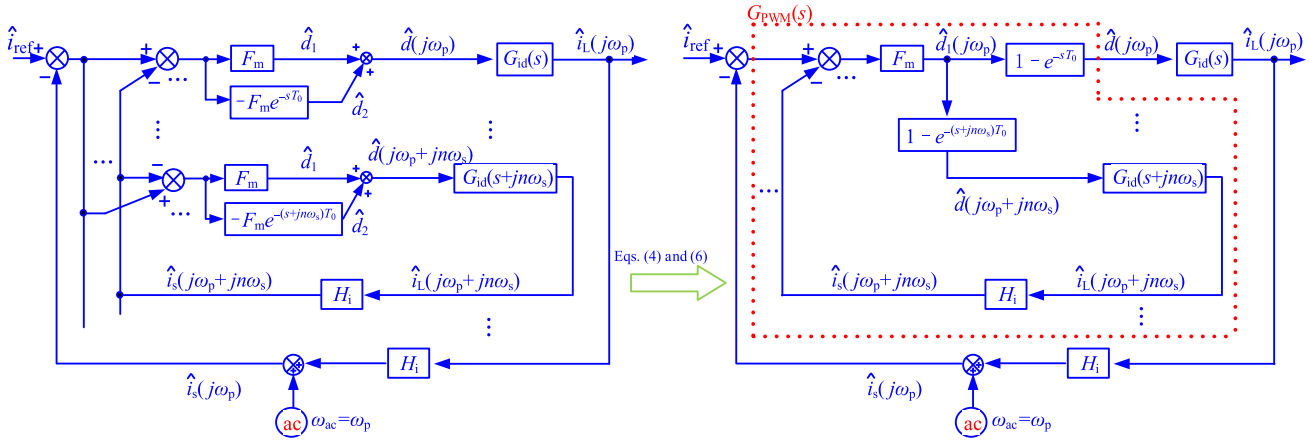

Fig. 4. Control block diagram of a C-COT/C-COFT controlled buck converter. $T_0 = T_{on}$ for C-COT and $T_0 = T_{off}$ for C-COFT.

i_s and I_{ref}, and the other part represented by $\hat{d}_2$ is another series of narrow pulse signals after T_{on} or T_{off} from each sampling instant.

Defining the ratio of $\hat{d}_1(k)$ to $\hat{i}_s(k)$ as $-F_m$, where $\hat{d}_1(k)$ and $\hat{i}_s(k)$ are the values of $\hat{d}_1$ and $\hat{i}_s$ at kT_s, respectively. Similar to the derivation process mentioned in Part I of this article, with the assumption of the small perturbation signal, it can be obtained that for C-COT

$$F_m = -\frac{\hat{d}_1(k)}{\hat{i}_s(k)} = \frac{1}{(m_2 - m_1)T_s/2} \tag{1}$$

and for C-COFT

$$F_m = -\frac{\hat{d}_1(k)}{\hat{i}_s(k)} = \frac{1}{(m_1 - m_2)T_s/2}. \tag{2}$$

In addition, the transfer function of the modulator $G_{PWM}(s)$ is defined as

$$G_{PWM}(s) \triangleq -\frac{\hat{d}(s)}{\hat{i}_s(s)}. \tag{3}$$

The expression of $G_{PWM}(s)$ will be derived in the following. If a C-COT/C-COFT controlled buck converter initially has an ac small perturbation signal with the angular frequency ω_p, then due to the sampling characteristic of the modulator, both $\hat{d}$ and $\hat{i}_s$ will contain the corresponding ac components at the frequencies $\omega_p + n\omega_s$ ($n = 0, \pm1, \pm2, \ldots$). Denoting $\hat{d}_1(j\omega)$, $\hat{d}_2(j\omega)$, $\hat{d}(j\omega)$ and $\hat{i}_s(j\omega)$ as the Fourier coefficients of $\hat{d}_1$, $\hat{d}_2$, $\hat{d}$, and $\hat{i}_s$ at ω, respectively, then using Shannon's sampling theorem, with the assumption of the small signal, we have

$$\hat{d}_1(j\omega_p) = \hat{d}_1(j\omega_p + jn\omega_s) = -F_m \sum_{n=-\infty}^{+\infty} \hat{i}_s(j\omega_p + jn\omega_s). \tag{4}$$

Also, from Figs. 2 and 3, we see that the relationships among $\hat{d}$, $\hat{d}_1$, and $\hat{d}_2$ are

$$\begin{cases} \hat{d}_2(t) = -\hat{d}_1(t - T_0) \\ \hat{d}(t) = \hat{d}_1(t) + \hat{d}_2(t) \end{cases} \tag{5}$$

where $T_0 = T_{on}$ for C-COT and $T_0 = T_{off}$ for C-COFT. Applying Fourier transform to (5) leads to

$$\begin{cases} \hat{d}_2(j\omega_p + jn\omega_s) = -\hat{d}_1(j\omega_p + jn\omega_s)e^{-(j\omega_p + jn\omega_s)T_0} \\ \hat{d}(j\omega_p + jn\omega_s) = \hat{d}_1(j\omega_p + jn\omega_s)\left(1 - e^{-(j\omega_p + jn\omega_s)T_0}\right). \end{cases} \tag{6}$$

According to (4), (6), and Fig. 1, the control block diagram for the C-COT/C-COFT controlled buck converter is depicted in Fig. 4, where $G_{id}(s)$ is the d-to-i_L transfer function. From Fig. 4, one can find that $G_{PWM}(s)$ can be derived as

$$\begin{aligned} G_{PWM}(s) &= -\frac{\hat{d}(s)}{\hat{i}_s(s)}\Big|_{s=j\omega_p} \\ &= \frac{F_m\left(1 - e^{-sT_0}\right)}{1 + F_m H_i \sum\limits_{\substack{n=-\infty \\ n\neq 0}}^{+\infty} G_{id}(s + jn\omega_s)\left(1 - e^{-(s+jn\omega_s)T_0}\right)}. \end{aligned} \tag{7}$$

According to Fig. 4, the loop gain is readily obtained as

$$T_i(s) = H_i G_{id}(s) G_{PWM}(s). \tag{8}$$

Obviously, the infinite series in (7) hinders the analysis of the sideband effect on the converter stability. As addressed in Part I, there are usually two methods to solve this problem, one of which is to consider only the influence of several most influential sideband components, and we can define $G_{PWM\_M}(s)$ and $T_{i\_M}(s)$ as the expressions of $G_{PWM}(s)$ and $T_i(s)$, respectively, when only the sideband components within the M multiples of the switching frequency range are considered. The other method is to eliminate the infinite series using some infinite sum formulas, thus obtaining a simple expression of $G_{PWM}(s)$, denoted as $G_{PWM\_a}(s)$. In this method, the expression of $G_{id}(s)$ in (7) should be replaced with its high frequency approximation first. At frequencies higher than the resonant frequency f_r of the power stage, $G_{id}(s)$ can be simplified to be a simple form, represented by $G_{id\_a}(s)$. For buck converter, the expressions of $G_{id}(s)$ and $G_{id\_a}(s)$ are

$$\begin{cases} G_{id}(s) = \frac{V_{in}(C_f s + 1/R_{Ld})}{L_f C_f s^2 + (L_f/R_{Ld} + R_c C_f)s + 1} \\ G_{id\_a}(s) = \frac{1}{H_i}\frac{m_1 + m_2}{s} = \frac{V_{in}}{sL_f}. \end{cases} \tag{9}$$

TABLE I
THEORETICAL MODELS FOR A C-COT OR C-COFT CONTROLLED BUCK CONVERTER

C-COT	C-COFT
$T_0=T_{\rm on}$, $T_{\rm s}=\frac{T_{\rm on}}{D}=\frac{V_{\rm in}}{V_{\rm o}}T_{\rm on}$, $F_{\rm m}=\frac{1}{(m_2-m_1)T_{\rm s}/2}$	$T_0=T_{\rm off}$, $T_{\rm s}=\frac{T_{\rm off}}{1-D}=\frac{V_{\rm in}}{V_{\rm in}-V_{\rm o}}T_{\rm off}$, $F_{\rm m}=\frac{1}{(m_1-m_2)T_{\rm s}/2}$
$G_{\rm PWM\_M}(s)=F_{\rm m}\frac{1-e^{-sT_0}}{1+F_{\rm m}H_{\rm i}\sum\limits_{\substack{n=-M\\ n\neq 0}}^{+M}G_{\rm id}(s+jn\omega_{\rm s})\left(1-e^{-(s+jn\omega_{\rm s})T_0}\right)}$, $G_{\rm PWM\_a}(s)=\frac{F_{\rm m}\left(1-e^{-sT_0}\right)}{1+F_{\rm m}H_{\rm i}\sum\limits_{\substack{n=-\infty\\ n\neq 0}}^{+\infty}G_{\rm id\_a}(s+jn\omega_{\rm s})\left(1-e^{-(s+jn\omega_{\rm s})T_0}\right)}=\frac{2L_{\rm f}}{H_{\rm i}V_{\rm in}T_0}\frac{1-e^{-sT_0}}{2\left(1-\frac{1-e^{-sT_0}}{sT_0}\right)}$	
$T_{\rm i\_M}(s)=H_{\rm i}G_{\rm id}(s)G_{\rm PWM\_M}(s)$, $T_{\rm i\_a}(s)=H_{\rm i}G_{\rm id}(s)G_{\rm PWM\_a}(s)$	

Then, using the following infinite sum formulas [10]

$$\begin{cases}\sum_{n=-\infty}^{+\infty}\frac{1}{n+x}=\pi\cot(\pi x)\\ \sum_{n=-\infty}^{+\infty}\frac{\sin((n+x)\theta)}{n+x}=\pi \qquad (0<\theta<2\pi,\ x\neq 0)\\ \sum_{n=-\infty}^{+\infty}\frac{\cos((n+x)\theta)}{n+x}=\pi\cot(\pi x)\end{cases} \tag{10}$$

the final expressions of $G_{\rm PWM\_a}(s)$ and $T_{\rm i\_a}(s)$ can be obtained, as tabulated in Table I. The detailed derivation process is similar to that in Part I, and is omitted here due to space limitation.

Correspondingly, the expressions of the closed-loop gain $T_c(s)$, i.e., the transfer function from $i_{\rm ref}$ to $i_{\rm s}$, can be derived based on either $T_{v\_M}(s)$ or $T_{v\_a}(s)$, and the obtained results, denoted as $T_{c\_M}(s)$ and $T_{c\_a}(s)$, respectively, are as follows:

$$\begin{aligned}T_{c\_M}(s)&=\frac{T_{i\_M}(s)}{1+T_{i\_M}(s)}\\&=\frac{F_mH_iG_{\rm id}(s)\left(1-e^{-sT_0}\right)}{1+F_mH_i\sum\limits_{n=-M}^{+M}G_{\rm id}(s+jn\omega_{\rm s})\left(1-e^{-(s+jn\omega_{\rm s})T_0}\right)}\end{aligned} \tag{11}$$

$$\begin{aligned}T_{c\_a}(s)&=\frac{T_{i\_a}(s)}{1+T_{i\_a}(s)}\\&=\frac{F_mH_iG_{\rm id}(s)\left(1-e^{-sT_0}\right)}{1+F_mH_i\left(G_{\rm id}(s)\left(1-e^{-sT_0}\right)+\sum\limits_{\substack{n=-\infty\\ n\neq 0}}^{+\infty}G_{\rm id\_a}(s+jn\omega_{\rm s})\left(1-e^{-(s+jn\omega_{\rm s})T_0}\right)\right)}.\end{aligned} \tag{12}$$

At frequencies higher than $f_{\rm r}$, (12) can be further simplified as (13), shown at the bottom of this page, by replacing $G_{\rm id}(s)$ with $G_{\rm id\_a}(s)$ and substituting the expression of F_m into it.

It should be noted that the low-frequency gain of $T_{i\_a}(s)$ is much greater than 1 no matter $G_{\rm id}(s)$ or $G_{\rm id\_a}(s)$ is used in (12), therefore the low-frequency gain of $T_{c\_a}(s)$ is very close to 1. That is to say, the result in (13) matches that in (12) even in the low frequency range. In [6], the expression of $T_c(s)$ of the C-COT or C-COFT controlled buck converter, represented by $T_{c\_{\rm Li}}(s)$, was obtained by using the DF method. It is found that the expression of $T_{c\_{\rm Li}}(s)$ in [6] is essentially equivalent to that given by (13), which implies $T_{c\_{\rm Li}}(s)$ is only a special case of the result obtained in this article. A proof of the equivalence is detailed in Appendix I with the C-COT control as an example.

B. Stability Analysis

We now undertake to analyze the effect of the sideband components on the converter stability with the C-COT control as an example. First, defining the factor related to "s" in $G_{{\rm PWM}\_a}(s)$ as $G_3(s)$, and further using the first-order Padé approximants for $e^{-sT{\rm on}}$, then, in the low-frequency range, we have

$$G_3(s)=\frac{1-e^{-sT_{\rm on}}}{2\left(1-\frac{1-e^{-sT_{\rm on}}}{sT_{\rm on}}\right)}\approx\frac{sT_{\rm on}}{2\left(1-\frac{sT_{\rm on}-\frac{1}{2}(sT_{\rm on})^2}{sT_{\rm on}}\right)}=1. \tag{14}$$

Fig. 5 shows the Bode plot of $G_3(s)$ when $T_{\rm on}$ is chosen as 3 μs, and the position of the switching frequency $f_{\rm s}$ with different values of duty cycle are also illustrated in this figure. Note when $D=1$, $f_{\rm s}$ reaches the maximum and is equal to $1/T_{\rm on}$. As demonstrated in Fig. 5, at frequencies below $0.5/T_{\rm on}$ the gain of $G_3(s)$ is 1, and the phase of $G_3(s)$ is above –90° in the entire frequency range.

In addition, according to the expression of $G_{{\rm PWM}\_a}(s)$ given in Table I, it can be concluded that in the C-COT/C-COFT control the sideband effect makes the low-frequency characteristic of the modulator behaves like a proportional gain, the value of which is $2L_f/H_iV_{\rm in}T_0$. In particular, the modulator can be regarded as a proportional gain in the entire switching frequency range when $D<0.5$. Given that the phase of $G_{\rm id}(s)$ at frequencies higher than f_r is –90°, one can deduce that the phase of the loop gain will be above –180°, thus explaining the phenomenon that a C-COT/C-COFT controlled buck converter is always stable at any duty cycle. In fact, this phenomenon can also be explained by observing that $T_{c\_a}(s)$ given in (13) contains no right half plane (RHP) pole.

$$\begin{aligned}T_{c\_a}(s)&\approx\frac{H_{\rm i}G_{\rm id\_a}(s)G_{\rm PWM\_a}(s)}{1+H_{\rm i}G_{\rm id\_a}(s)G_{\rm PWM\_a}(s)}=\frac{H_iG_{\rm id\_a}(s)\left(1-e^{-sT_0}\right)}{\frac{1}{F_m}+H_i\sum\limits_{n=-\infty}^{+\infty}G_{\rm id\_a}(s+jn\omega_{\rm s})\left(1-e^{-(s+jn\omega_{\rm s})T_0}\right)}\\&=\frac{H_{\rm i}G_{\rm id\_a}(s)\left(1-e^{-sT_0}\right)}{\frac{1}{F_m}+(m_1+m_2)\sum\limits_{n=-\infty}^{+\infty}\frac{1-e^{-(s+jn\omega_{\rm s})T_0}}{s+jn\omega_s}}=\frac{H_{\rm i}G_{\rm id\_a}(s)\left(1-e^{-sT_0}\right)}{\frac{1}{F_m}+(m_1+m_2)\frac{\pi}{\omega_s}}=\frac{1-e^{-sT_0}}{sT_0}\end{aligned} \tag{13}$$

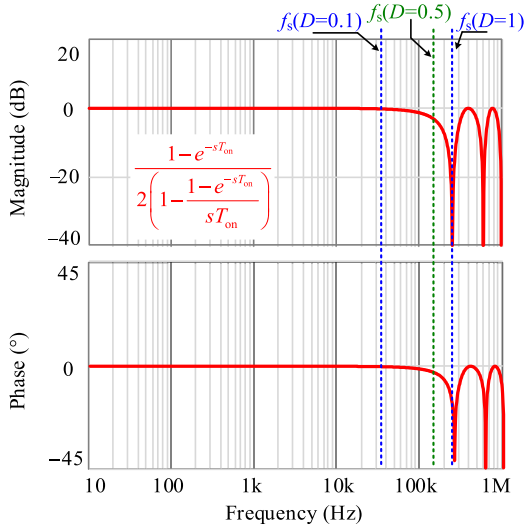

Fig. 5. Bode plot of $G_3(s)$ with $T_{on} = 3\ \mu s$.

TABLE II
SIMULATED BUCK CONVERTER PARAMETERS

Parameters	Symbols	Values	Parameters	Symbols	Values
Input voltage	V_{in} / V	12	Inductance	L_f / μH	6
Output voltage	V_o / V	3.3	Output capacitance	C_f / μF	100
Output power	P_o / W	33	ESR	R_c / mΩ	10
Load	R_{Ld} / Ω	1/3	Current sensed gain	H_i	0.1

C. Simulation Verification

To demonstrate the correctness of the proposed theoretical models, a C-COT controlled buck converter is simulated in Simplis, and the circuit parameters are given in Table II, where T_{on} is chosen as 3 μs. It can be calculated that f_s is about 98 kHz in this case.

Fig. 6 shows the comparisons of the theoretical models with the simulated results. $G_{PWM\_10}(s)$ and $T_{i\_10}(s)$ represent the expressions of $G_{PWM\_M}(s)$ and $T_{i\_M}(s)$ given in Table I when $M = 10$, respectively. As seen, $G_{PWM\_a}(s)$ and $T_{i\_a}(s)$ given in Table I agree well with the corresponding simulated results in the entire frequency range except for a small difference close to the switching frequency and its multiples, and this difference can be ignored in practical application.

Furthermore, it can be found that there is a distinct difference between $G_{PWM\_10}(s)$ or $T_{i\_10}(s)$ and the corresponding simulated result, which further indicates that all the sideband components have a non-negligible influence on the low-frequency gain of the modulator in the C-COT/C-COFT control.

III. SAMPLED-DATA MODELING FOR V-COT/V-COFT

In this section, the small-signal models of a V-COT/V-COFT controlled buck converter are given first by using the same modeling process in Section II, and the obtained results are further simplified to analyze the sideband effect on the low-frequency characteristic of the modulator and the converter stability followed up with the simulation verifications.

A. Sampled-Data Modeling

Fig. 7 shows a V-COT/V-COFT controlled buck converter and the representations of the circuit variables are the same as those in Fig. 1. Besides, v_o and v_{fb} are the output voltage and the voltage feedback respectively, H_v is the voltage sensor gain, implemented by the divider consists of resistors R_1 and R_2. The part from v_{fb} to d is referred to as the modulator.

Fig. 8 shows the operating principle of the modulator at steady state, which is the same as that in Figs. 2 and 3. Similar to (3), in the V-COT and V-COFT controls, the transfer function of the modulator $G_{PWM}(s)$ is defined as

$$G_{PWM}(s) \triangleq -\frac{\hat{d}(s)}{\hat{v}_{fb}(s)}. \tag{15}$$

Then, with reference to the derivation process in Section II, the expression of $G_{PWM}(s)$ for a V-COT/V-COFT controlled buck converter can be obtained as

$$G_{PWM}(s) = \frac{F_m\left(1-e^{-sT_0}\right)}{1+F_m H_v \sum\limits_{\substack{n=-\infty \\ n\neq 0}}^{+\infty} G_{vd}(s+jn\omega_s)\left(1-e^{-(s+jn\omega_s)T_0}\right)} \tag{16}$$

where $T_0 = T_{on}$ for V-COT and $T_0 = T_{off}$ for V-COFT, the derivation of F_m and the obtained expression are both the same as those in peak/valley voltage mode control, which can be found in Part I, and $G_{vd}(s)$ is the d-to-v_o transfer function. In the frequency range higher than f_r, $G_{vd}(s)$ can be simplified to be a simple form, represented by $G_{vd\_a}(s)$, these two expressions have been given in the first part, and are rewritten as follows.

$$\begin{cases} G_{vd}(s) = V_{in}\frac{R_cC_fs+1}{L_fC_fs^2+(L_f/R_{Ld}+R_cC_f)s+1} \\ G_{vd\_a}(s) = V_{in}\frac{R_cC_fs+1}{L_fC_fs^2} = \frac{V_{in}}{L_fC_f}\left(\frac{R_cC_f}{s}+\frac{1}{s^2}\right). \end{cases} \tag{17}$$

Similar to the simplification method given in Section II, defining $G_{PWM\_M}(s)$ and $T_{i\_M}(s)$ as the expressions of $G_{PWM}(s)$ and $T_i(s)$, respectively, when only the sideband components within the M multiples of the switching frequency range are considered, and defining $G_{PWM\_a}(s)$ and $T_{i\_a}(s)$ as the expressions of $G_{PWM}(s)$ and $T_i(s)$, respectively, when $G_{vd}(s)$ in (16) is replaced by $G_{vd\_a}(s)$. Then, using the following infinite sum formulas:

$$\begin{cases} \sum_{n=-\infty}^{+\infty}\frac{1}{(n+x)^2} = \frac{\pi^2}{\sin^2(\pi x)} \\ \sum_{n=-\infty}^{+\infty}\frac{\cos((n+x)\theta)}{(n+x)^2} = -\pi\theta+\frac{\pi^2}{\sin^2(\pi x)}(0<\theta<2\pi, x\neq 0) \\ \sum_{n=-\infty}^{+\infty}\frac{\sin((n+x)\theta)}{(n+x)^2} = \theta\pi\cot(\pi x) \end{cases} \tag{18}$$

the expressions of $G_{PWM\_a}(s)$ and $T_{v\_a}(s)$ can be further simplified to the results as given in Table III.

Correspondingly, the closed-loop gain $T_c(s)$, i.e., the transfer function from v_{ref} to v_{fb}, can be derived based on either $T_{v\_M}(s)$

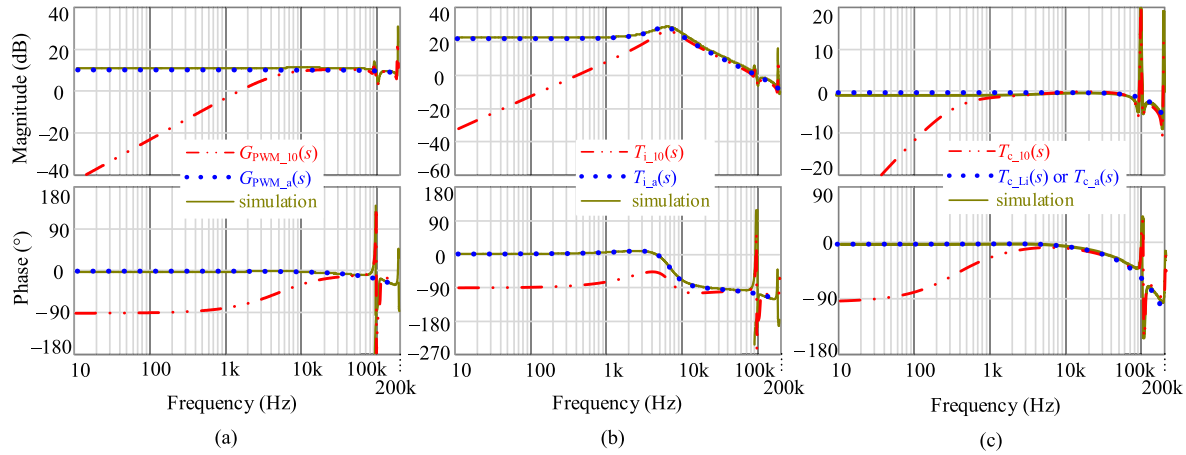

Fig. 6. Comparison between theoretical models and simulation results for a C-COT controlled buck converter. (a) G_{PWM}. (b) T_i. (c) T_c.

TABLE III
THEORETICAL MODELS FOR A V-COT OR V-COFT CONTROLLED BUCK CONVERTER

V-COT	V-COFT
$T_0=T_{on}$, $T_s=\frac{T_{on}}{D}=\frac{V_{in}}{V_o}T_{on}$, $F_m=\frac{1}{H_v\left(R_c\frac{m_2-m_1}{2}+\frac{m_1DT_s}{2C_f}\right)T_s}$	$T_0=T_{off}$, $T_s=\frac{T_{off}}{1-D}=\frac{V_{in}}{V_{in}-V_o}T_{off}$, $F_m=\frac{1}{H_v\left(R_c\frac{m_1-m_2}{2}+\frac{m_1DT_s}{2C_f}\right)T_s}$

$$G_{PWM\_M}(s)=F_m\frac{1-e^{-sT_0}}{1+F_mH_v\sum_{\substack{n=-M\\n\neq0}}^{+M}G_{vd}(s+jn\omega_s)\left(1-e^{-(s+jn\omega_s)T_0}\right)},\quad T_{v\_M}(s)=H_vG_{vd}(s)G_{PWM\_M}(s)$$

$$G_{PWM\_a}(s)=\frac{F_m\left(1-e^{-sT_0}\right)}{1+F_mH_v\sum_{\substack{n=-\infty\\n\neq0}}^{+\infty}G_{vd\_a}(s+jn\omega_s)\left(1-e^{-(s+jn\omega_s)T_0}\right)}=\frac{F_m\left(1-e^{-sT_0}\right)}{1+\frac{F_mH_vV_{in}}{L_fC_f}\left(R_cC_f\left(\frac{\pi}{\omega_s}-\frac{1-e^{-sT_0}}{s}\right)-\frac{1-e^{-sT_0}}{s^2}-\frac{\pi T_0}{\omega_s}+\frac{T_0\pi\cot(\pi\frac{s}{j\omega_s})}{j\omega_s}\right)},\quad T_{v\_a}(s)=H_vG_{vd}(s)G_{PWM\_a}(s)$$

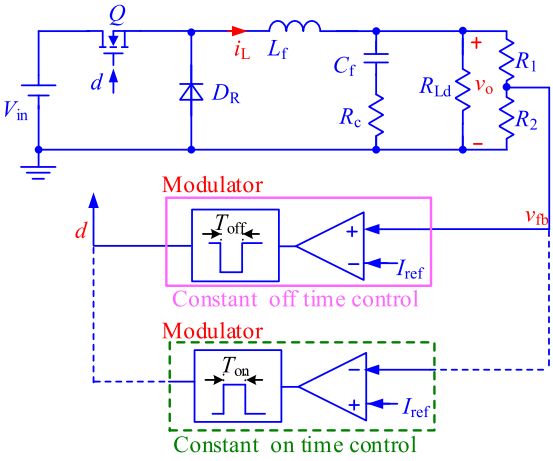

Fig. 7. V-COT/V-COFT controlled buck converter. The power stage and the modulator are connected by the solid lines under V-COT and the dashed lines under V-COFT.

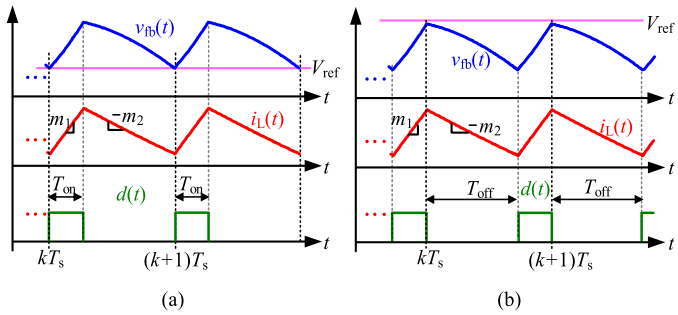

Fig. 8. Key waveforms of the modulator in steady state. (a) V-COT. (b) V-COFT.

or $T_{v\_a}(s)$, and the obtained results are denoted as $T_{c\_M}(s)$ and $T_{c\_a}(s)$ respectively, which are defined as

$$T_{c\_M}(s)=\frac{T_{v\_M}(s)}{1+T_{v\_M}(s)}$$

$$=\frac{F_mH_vG_{vd}(s)\left(1-e^{-sT_0}\right)}{1+F_mH_v\sum_{n=-M}^{+M}G_{vd}(s+jn\omega_s)\left(1-e^{-(s+jn\omega_s)T_0}\right)} \tag{19}$$

$$T_{c\_a}(s)=\frac{T_{v\_a}(s)}{1+T_{v\_a}(s)}$$

$$=\frac{F_mH_vG_{vd}(s)\left(1-e^{-sT_0}\right)}{1+F_mH_v\left(G_{vd}(s)\left(1-e^{-sT_0}\right)+\sum_{\substack{n=-\infty\\n\neq0}}^{+\infty}G_{vd\_a}(s+jn\omega_s)\left(1-e^{-(s+jn\omega_s)T_0}\right)\right)}. \tag{20}$$

At frequencies higher than f_r, (20) can be further simplified as the form in (21), shown at the bottom of the next page, by replacing $G_{\rm vd}(s)$ with $G_{{\rm vd}\_a}(s)$ and substituting the expression of F_m into it. Note that the low frequency gain of T_c(s) is very close to 1 no matter $G_{\rm vd}(s)$ or $G_{{\rm vd}\_a}(s)$ is used in (20), which is similar to the scenario in the C-COT/C-COFT control and also suggests that the result in (21) has good agreement with that in (20) even in the low frequency range. However, this does not mean that the modeling process of (21) is effective at low frequencies.

In [6], the assumption that the perturbation signal in the voltage across the ESR of the output capacitor remains unchanged during the switch ON-time and OFF-time is introduced into the derivation process of the closed-loop gain, represented by $T_{c\_{\rm Li}}(s)$ here. In fact, this assumption is only true in the high-frequency range. Besides, $T_{c\_{\rm Li}}(s)$ is the same as the result in (21) after rearrangement, and a proof of the equivalence is detailed in Appendix I with the V-COT control as an example.

B. Stability Analysis

The stability can be easily determined by examining the existence of RHP poles in $T_{c\_a}(s)$. First, defining the term "cot($\pi s/j\omega_s$)" in $G_{{\rm PWM}\_a}(s)$ as $G_4(s)$, and at frequencies below $0.5f_s$, we have

$$G_4(s)=\frac{\pi}{j\omega_s}\cot\left(\pi\frac{s}{j\omega_s}\right)\approx\frac{1}{s}+\frac{1}{3}s\frac{\pi^2}{{\omega_s}^2}. \tag{22}$$

Using the Taylor expansion for $e^{-sT_{\rm s}}$, $G_{{\rm PWM}\_a}(s)$ can then be simplified in the low-frequency region as

$$G_{{\rm PWM}\_a}(s)\approx\frac{2L_fC_f}{H_vV_{\rm in}\left(R_cC_fT_0-\frac{1}{3}T_0^2+\frac{1}{6}T_s^2\right)} \tag{23}$$

from which, we can calculate the low-frequency gain of the modulator. In addition, according to (21) and (22), one can find that at frequencies below $0.5f_s$

$$T_{c\_a}(s)\approx\frac{1}{T_0}\left(\frac{R_cC_f}{s}+\frac{1}{s^2}\right)\frac{1-e^{-sT_0}}{R_cC_f-\frac{T_0}{2}+\frac{1}{s}+\frac{1}{3}s\frac{\pi^2}{{\omega_s}^2}} \tag{24}$$

which indicates that $T_{c\_a}(s)$ has two RHP poles if the product of R_c and C_f is less than $0.5T_0$. That is to say, for the V-COT or V-COFT controlled buck converter, the time constant R_cC_f of the output capacitor needs to satisfy

$$R_cC_f>\frac{T_0}{2}. \tag{25}$$

In some practical applications, a ramp compensation signal is added into the feedback signal to ensure the stable operation of the buck converter with the V-COT control. In these cases, the expression of F_m is still the same as that in the VVM control with $m_c\neq 0$, then the selection range of m_c can also be obtained by using the same analysis as above.

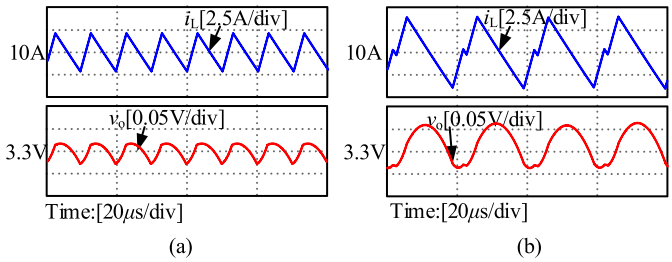

Fig. 9. Simulated waveforms of a V-COT controlled buck converter. (a) Rc=10 mΩ. (b) Rc=5 mΩ.

C. Simulation Verification

To demonstrate the correctness of the above theoretical models, a V-COT controlled buck converter is simulated in Simplis, and the circuit parameters have been given in Table II except that $C_f=200$ μF, $R_c=10$ mΩ or 5 mΩ, $R_1=2.1$ kΩ, and $R_2=1.2$ kΩ. Moreover, $T_{\rm on}$ is chosen as 3 μs, and f_s is about 98 kHz in this case. Different values of R_c are used in order to explain the instability phenomenon of a V-COT controlled buck converter with the smaller time constant C_fR_c.

Fig. 9 shows the simulated time-domain waveforms when two different $R_{\rm c}$ are used. As seen, the converter is unstable when $R_c=5$ mΩ, but turns stable when $R_c=10$ mΩ, as predicted by (25). Figs. 10 and 11 show the comparisons of the theoretical models with the simulated results when different R_c are used. As demonstrated, $G_{{\rm PWM}\_a}(s)$ and $T_{v\_a}(s)$ given in Table III and $T_{c\_a}(s)$ given by (21) agree well with the corresponding simulated results except for a small discrepancy at the frequencies close to the switching frequency and its multiples. Furthermore, $G_{{\rm PWM}\_10}(s)$, $T_{v\_10}(s)$, and $T_{c\_10}(s)$ are found to have a big deviation from the simulation results, which indicates that the sideband components have a significant effect on the low-frequency gain of the modulator.

It can also be found from Fig. 11(b) that the cut-off frequency of the loop gain is close to $0.5f_s$ and the phase margin is negative when $R_c=5$ mΩ, which is consistent with the unstable phenomenon observed in Fig. 9(b). In contrast, Fig. 10(b) shows that the cut-off frequency is about $0.5f_s$, and the phase margin is positive, indicating the converter is stable when $R_c=10$ mΩ, which matches the stable case shown in Fig. 9(a).

$$T_{c\_a}(s)\approx\frac{F_mH_vG_{{\rm vd}\_a}(s)\left(1-e^{-sT_0}\right)}{1+F_mH_v\sum\limits_{n=-\infty}^{+\infty}G_{{\rm vd}\_a}(s+jn\omega_s)\left(1-e^{-(s+jn\omega_s)T_0}\right)}=\frac{G_{{\rm vd}\_a}(s)\left(1-e^{-sT_0}\right)}{\frac{1}{F_mH_v}+\sum\limits_{n=-\infty}^{+\infty}G_{{\rm vd}\_a}(s+jn\omega_s)\left(1-e^{-(s+jn\omega_s)T_0}\right)}$$
$$=\frac{G_{{\rm vd}\_a}(s)\left(1-e^{-sT_0}\right)}{\frac{1}{F_mH_v}+\frac{V_{\rm in}}{L_fC_f}\left(\sum\limits_{n=-\infty}^{+\infty}\frac{R_cC_f\left(1-e^{-(s+jn\omega_s)T_0}\right)}{s+jn\omega_s}+\sum\limits_{n=-\infty}^{+\infty}\frac{1-e^{-(s+jn\omega_s)T_0}}{(s+jn\omega_s)^2}\right)}=\frac{1}{T_0}\left(\frac{R_cC_f}{s}+\frac{1}{s^2}\right)\frac{1-e^{-sT_0}}{R_cC_f-\frac{T_0}{2}+\frac{\pi}{j\omega_s}\cot\left(\pi\frac{s}{j\omega_s}\right)} \tag{21}$$

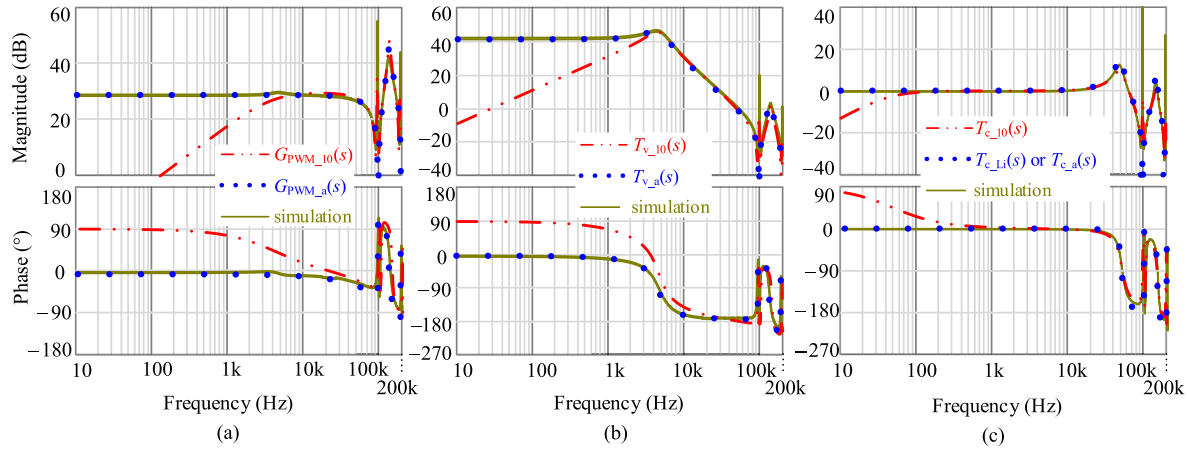

Fig. 10. Comparison between theoretical models and simulation results for a V-COT controlled buck converter with $T_{on} = 3\ \mu s$ and $R_c = 10\ m\Omega$. (a) G_{PWM}. (b) T_v. (c) T_c.

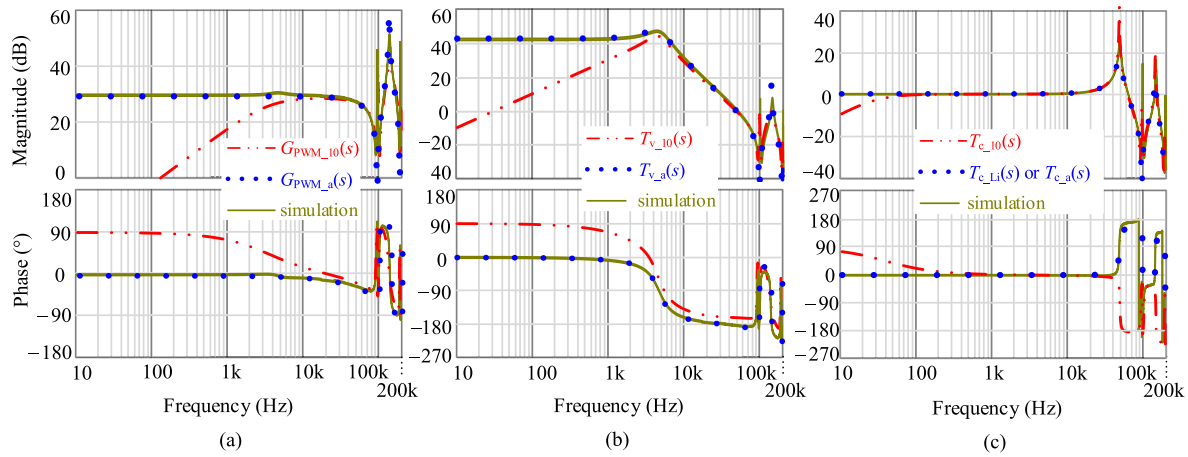

Fig. 11. Comparison between theoretical models and simulation results for a V-COT controlled buck converter with $T_{on} = 3\ \mu s$ and $R_c = 5\ m\Omega$. (a) G_{PWM}. (b) T_v. (c) T_c.

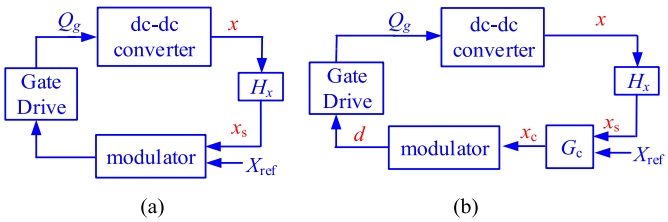

Fig. 12. Block diagrams of the dc-dc converter under different control schemes. (a) Ripple-based control. (b) AVM/ACM control.

IV. Discussion

This section will discuss the unification of the modeling methods for ripple-based control and average control, as well as the applicability of the sampled-data modeling method for other types of dc–dc converters.

Fig. 12 shows the block diagrams of the dc–dc converters with ripple-based control and AVM/ACM control, where x represents the variable to be sensed, x_s and x_c represent the feedback signal and the control signal respectively, H_x represents the gain of the sensor. Note that there is a compensator G_c in Fig. 12(b), but it is absent in Fig. 12(a).

In the control schemes shown in Fig. 12, the transfer functions of the modulator are all derived based on the sampling characteristic of the modulator with some differences in the modeling process, mainly including the following.

1) The modulator behaves like a negative feedback subsystem at steady state in Fig. 12(a), i.e., the larger x, the smaller the d. However, the modulator in Fig. 12(b) is a positive feedback subsystem.

2) For AVM/ACM, the slope of x_c at the sampling instant can be ignored in the modeling process due to the small switching ripple in x_c, which is caused by the attenuation of the controller at high frequencies. However, when ripple-based control is adopted, the bandwidth of the loop gain is usually located in the high-frequency range, where the switching ripple of the input signal of the modulator cannot be ignored. Therefore, in this case, the slope of x_s at the sampling instant and the sideband effect need to be considered in the modeling process.

The proposed sampled-data modeling method can also be applied to boost/buck–boost converter, except the case when

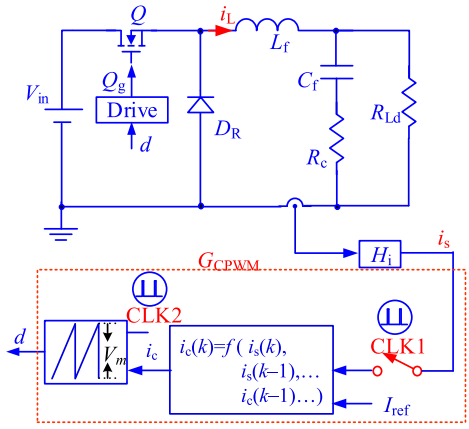

Fig. 13. Buck converter with the digital current-mode control.

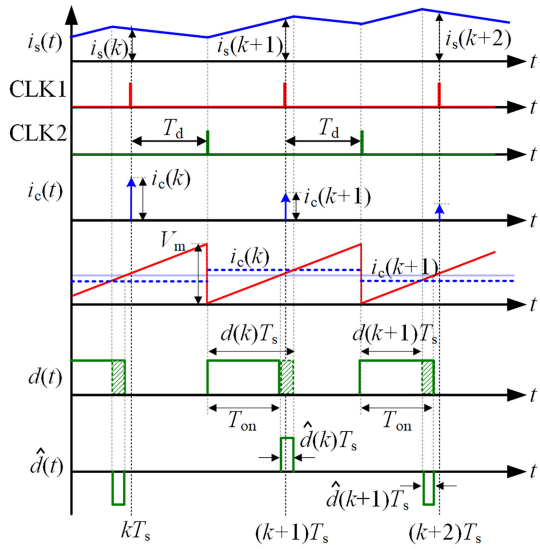

Fig. 14. Key waveforms of the circuit shown in Fig. 13 in the perturbed state.

the output capacitor has a large ESR in the voltage-mode ripple-based control, and the exact expression of $G_{\rm id}(s)$ or $G_{\rm vd}(s)$ is required in the modeling process, which has been explained in Part I with the PCM control as an example.

V. Extension of the Sampled-Data Modeling Method to Digital Control

According to the modeling process developed in this article, it can be found that the transfer functions of the modulators in the ripple-based control can be obtained by using the sampling theorem as long as $\hat{d}(t)$ can be expressed in terms of the feedback signal $\hat{x}(t)$ and $\delta(t)$. In a digitally controlled dc-dc converter, the relationship between the perturbation components in the duty cycle and the sensed signal is similar to that between $\hat{d}_2$ and $\hat{i}_{\rm s}$ in Figs. 2 and 3. Based on this characteristic, it can be inferred that a digital dc-dc converter can also be regarded as a continuous system to analyze the stability or other performance, which provides a new way to analyze the performance of the digital systems directly in the *s*-domain rather than in the *z*-domain. This section will take a digitally controlled current-mode buck converter with a PI controller as an example to illustrate this issue.

A. Sampled-Data Modeling

Fig. 13 shows a digitally current-mode controlled buck converter with the trailing edge modulation, and the representations of the circuit variables are the same as those shown in Fig. 1. Besides, CLK1 represents the time instant at which i_s is sampled, i.e., the sampling instant, and CLK2 represents the time instant at which the switch is turned ON or the PWM carrier starts to rise in each switching period. For ease of analysis, the sampling instant is regarded as the beginning time in each switching period.

In the converter shown in Fig. 13, the part from i_s to d is usually implemented inside the microprocessor and can be divided into two parts, the first part is a digital controller with the input being the feedback current $i_{\rm s}$ and the output being the control signal $i_{\rm c}$. The other part is a digital PWM circuit where i_c compares with the carrier wave with a peak-to-peak value V_m to generate the duty cycle signal d. Let $G_{\rm CPWM}(s)$ denote the transfer function from i_s to d in the *s*-domain, and the subscript "$_{\rm CPWM}$" means that it is a combination of the transfer function of the controller and the modulator, i.e.,

$$G_{\rm CPWM}(s) \triangleq -\frac{\hat{d}(s)}{\hat{i}_s(s)}. \tag{26}$$

Fig. 14 shows the operating principle of the circuit in Fig. 13. At kT_s, i_s is sampled, then the sampled value $i_s(k)$ combined with the controller parameters k_p and k_i, is used to calculate the value of the control signal, represented by $i_c(k)$. T_d represents the time interval between CLK1 and CLK2. At kT_s+T_d, the switch turns ON and remains ON-state until $i_c(k)$ intersects the PWM carrier. Note that the calculation time is assumed to be zero, and it would not affect the theoretical models of the converter.

Defining $G_c(z)$ as the small-signal model of the digital controller in the *z*-domain, i.e.,

$$G_c(z) \triangleq -\frac{\hat{i}_c(z)}{\hat{i}_s(z)} = k_p + \frac{k_i T_s}{1-z^{-1}}. \tag{27}$$

Then, we have

$$\hat{i}_c(k) - \hat{i}_c(k-1) = -(k_p + k_i T_s)\,\hat{i}_s(k) + k_p \hat{i}_s(k-1) \tag{28}$$

and it can be written in another form, i.e.,

$$\begin{aligned}&\hat{i}_{\rm c}(t) - \hat{i}_{\rm c}(t-T_{\rm s})\\ &= -(k_{\rm p} + k_{\rm i}T_{\rm s})\hat{i}_{\rm s}(t)\delta_{T_{\rm s}}(t) + k_{\rm p}\hat{i}_{\rm s}(t-T_{\rm s})\delta_{T_{\rm s}}(t)\end{aligned} \tag{29}$$

where

$$\delta_{T_{\rm s}}(t) = \sum_{n=-\infty}^{+\infty} \delta(t - kT_s) \tag{30}$$

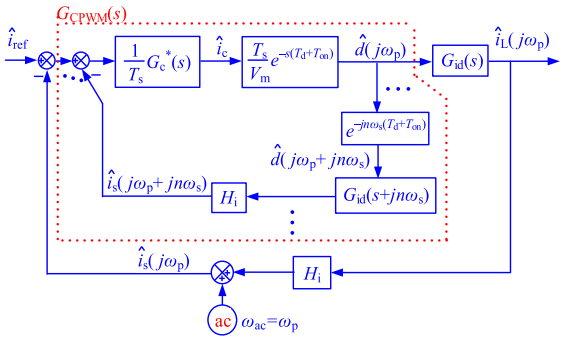

Fig. 15. Control block diagram of a digitally controlled dc–dc converter.

and $\delta(t)$ is Dirac delta function. Besides, according to Fig. 14, we have

$$\hat{d}(t)=\sum_{k=-\infty}^{+\infty}\hat{d}(k)T_s=\sum_{k=-\infty}^{+\infty}\frac{\hat{i}_c(k)}{V_m}T_s=\frac{\hat{i}_c(t-T_d-T_{\rm on})}{V_m}T_s. \tag{31}$$

Performing Fourier transform on (29) and (31) yields

$$\begin{aligned}\hat{i}_{\rm c}(s)(1-e^{-sT_s})&=\hat{i}_{\rm c}(s+jn\omega_s)(1-e^{-(s+jn\omega_s)T_s})\\&=-\tfrac{1}{T_s}\sum_{n=-\infty}^{+\infty}\left(\left(k_p+k_iT_s-k_pe^{-sT_s}\right)\hat{i}_s(s+jn\omega_s)\right)\end{aligned} \tag{32}$$

$$\hat{d}(s)=\frac{\hat{i}_c(s)e^{-s(T_d+T_{\rm on})}}{V_m}T_s \tag{33}$$

and (32) can be rewritten as

$$\hat{i}_c(s)=\hat{i}_c(s+jn\omega_s)=-\frac{1}{T_s}G_c^*(s)\sum_{n=-\infty}^{+\infty}\hat{i}_s(s+jn\omega_s) \tag{34}$$

where

$$\begin{aligned}G_c^*(s)&=\frac{k_p-k_pe^{-sT_s}+k_iT_{\rm s}}{1-e^{-sT_s}}=k_p+\frac{k_iT_{\rm s}}{1-e^{-sT_s}}\\&=G_c(z)\,|_{z=e^{sT_s}}\ .\end{aligned} \tag{35}$$

From (33) and (34), we see that

$$\begin{aligned}\hat{d}(s+jn\omega_s)&=\frac{\hat{i}_c(s+jn\omega_s)e^{-(s+jn\omega_s)(T_d+T_{\rm on})}}{V_m}T_s\\&=\frac{\hat{i}_c(s)e^{-s(T_{\rm d}+T_{\rm on})}e^{-jn\omega_{\rm s}(T_d+T_{\rm on})}}{V_m}T_s\\&=\hat{d}(s)e^{-jn\omega_{\rm s}(T_d+T_{\rm on})}.\end{aligned} \tag{36}$$

According to (33), (34), (36), and Fig. 13, the control block diagram of the converter shown in Fig. 13 can be obtained as depicted in Fig. 15, from which $G_{\rm CPWM}(s)$ can be derived as

$$G_{\rm CPWM}(s)=-\frac{\hat{d}(s)}{\hat{i}_{\rm s}(s)}\,|_{s=j\omega_p}=-\frac{\hat{i}_c(s)}{\hat{i}_s(s)}\frac{e^{-s(T_d+T_{\rm on})}}{V_m}T_s$$

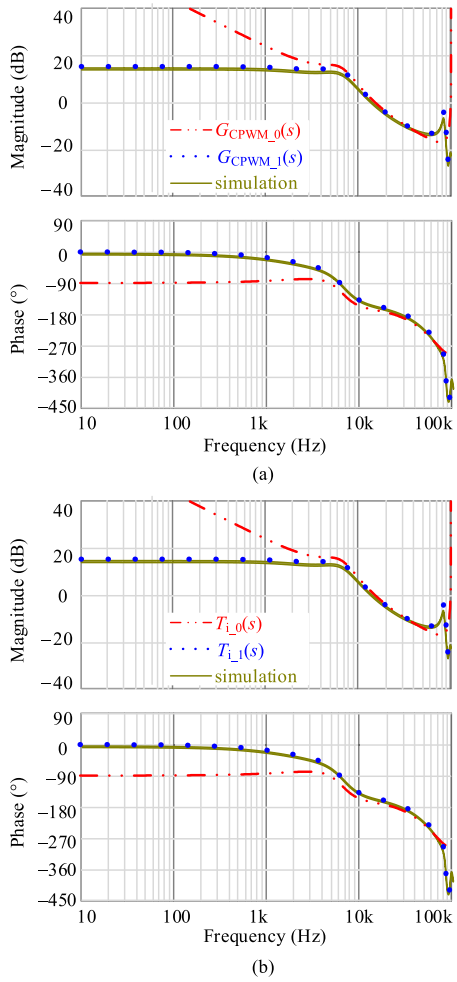

Fig. 16. Comparison between theoretical models and simulation results for a digitally current-mode controlled buck converter. $G_{\rm CPWM\_1}(s)$ or $T_{i\_1}(s)$ represents the expression of $G_{\rm CPWM}(s)$ or $T_i(s)$ when $M=1$, and $G_{\rm CPWM\_0}(s)$ or $T_{i\_0}(s)$ represents the expression of $G_{\rm CPWM}(s)$ or $T_i(s)$ when the sideband effect is not considered. (a) $\rm G_{CPWM}$. (b) $\rm T_i$.

$$=\frac{\frac{1}{V_m}G_c^*(s)e^{-s(T_d+T_{\rm on})}}{1+\frac{H_iG_c^*(s)}{V_m}\sum\limits_{\substack{n=-\infty\\n\neq0}}^{+\infty}G_{\rm id}(s+jn\omega_s)e^{-(s+jn\omega_s)(T_d+T_{\rm on})}}. \tag{37}$$

In addition, the loop gain $T_{\rm i}(s)$ is given as

$$T_{\rm i}(s)=H_iG_{\rm CPWM}(s)G_{\rm id}(s). \tag{38}$$

Similar to the previous analysis, letting $G_{\rm CPWM\_M}(s)$ and $T_{i\_\rm M}(s)$ represent the expressions of $G_{\rm CPWM}(s)$ and $T_i(s)$, respectively, when only the sideband components within the M multiples of the switching frequency range are considered.

B. Simulation Verification

To demonstrate the validity of the proposed method, a digitally current-mode controlled buck converter with a PI controller is simulated in Simplis, and the circuit parameters are the same as those given in Table II. Besides, $V_m=1.2$ V, $T_d=5$ μs, $k_p=0.2$, and $k_i=31420$. It should be noted that the analog signal

injection measurement, rather than the digital signal injection measurement, is used here.

Fig. 16 shows the comparison of the theoretical models with the simulated results. As demonstrated, $G_{\mathrm{CPWM\_1}}(s)$ and $T_{i\_1}(s)$ agree well with the corresponding simulated results in the entire switching frequency range, but there is a distinct difference between $G_{\mathrm{CPWM\_0}}(s)$ or $T_{i\_0}(s)$ and the simulated result, thus confirming the correctness of the modeling method proposed in this section and indicating the importance of considering the sideband effect in analyzing the stability of the digitally controlled converter.

It is worth reminding that the proposed models can be further used to analyze the effect of T_d and control parameters on the converter stability, but it is omitted here due to limited space. Moreover, perhaps the most important consequence of the proposed modeling technique is that one can treat a digital converter as an analog system, thus allowing us to model and analyze the digitally controlled converters in the s-domain, rather than in the z-domain [11]–[14] with the complicated derivation. Also, analog injection, which outperforms digital injection in general [15], can be used to measure the loop gain for a digitally controlled system.

VI. Conclusion

This section presents the sampled-data modeling method for the COT/COFT control. Compared with the modeling procedure for the constant frequency control in the previous part, it can be found that in a COT/COFT controlled dc–dc converter, the duty cycle perturbation signal contains not only a series of narrow pulse signals at each sampling instant, but also another series of pulse signals at a fixed time from each sampling point. By establishing the relationship between these two series of signals and using the sampling theorem, the transfer functions of the modulator and the loop gain are obtained, and they are further used to analyze the influence of the sideband components on the frequency response of the modulator and the loop gain. Finally, the simulation results verify the validity of the modeling methods proposed in this part.

It is demonstrated that the proposed sampled-data modeling method for ripple-based control is consistent with the multifrequency modeling method proposed in the existing literature for AVM, and these two methods are both based on the sampling characteristic of the modulator, thus providing us a unified understanding of the modeling techniques for the different basic control schemes. Another important significance of the proposed method is that it can be extended to the digital control, making it possible to analyze the performance of the digital systems in the same way as the analog systems which are more familiar to the researchers and engineers.

Perhaps, the insights that have emerged from the proposed sampled-data modeling method suggest that the influence of the sideband effect on the system stability is yet to be conceived, particularly in the high-bandwidth dc–dc converters and the cascade/parallel converters. The research on this subject well combined the instability phenomena and the new modeling theory, which promises to yield some simpler and more effective solutions to improve the performance of dc–dc converters.

Appendix I

This appendix intends to prove the equivalence between the closed-loop gains obtained by Li [6] and the results in (13) and (21) with the C-COT and V-COT control as an example.

In [6], the original forms of the closed-loop gains for the buck converter with the C-COT and V-COT controls ($H_v \neq 1$) (see (2.26) and (4.10) in [6]) are repeated in (A1) and (A2), respectively, below. It can be found that, after rearranging, the results in [6] are exactly the same with (13) and (21).

$$T_{c\_\mathrm{Li}}(s) = \frac{\hat{i}_s(s)}{\hat{i}_{\mathrm{ref}}(s)} = H_i \frac{f_s\left(1-e^{-sT_{\mathrm{on}}}\right)}{m_2}\frac{V_{\mathrm{in}}}{L_f s} = \frac{\left(1-e^{-sT_{\mathrm{on}}}\right)}{sT_{\mathrm{on}}} \tag{A1}$$

$$\begin{aligned} T_{c\_\mathrm{Li}}(s) = \frac{\hat{v}_{\mathrm{fb}}(s)}{\hat{v}_{\mathrm{ref}}(s)} &= \frac{f_s}{R_c m_2}\frac{\left(1-e^{-sT_{\mathrm{on}}}\right)\left(1-e^{-sT_s}\right)\frac{V_{\mathrm{in}}\left(R_cC_f s+1\right)}{L_f C_f s^2}}{\left(1+\frac{T_{\mathrm{off}}}{2R_cC_f}\right)-\left(1-\frac{2T_{\mathrm{on}}+T_{\mathrm{off}}}{2R_cC_f}\right)e^{-sT_s}} \\ &= \frac{V_{\mathrm{in}}(R_cC_f s+1)}{T_s m_2 L_f C_f s^2} C_f \frac{\left(1-e^{-sT_{\mathrm{on}}}\right)\left(1-e^{-sT_s}\right)}{R_cC_f+\frac{T_{\mathrm{off}}}{2}-\left(R_cC_f-\left(T_s-\frac{D'T_s}{2}\right)\right)e^{-sT_s}} \\ &= \frac{V_{\mathrm{in}}(R_cC_f s+1)}{T_s m_2 L_f C_f s^2} C_f \frac{1-e^{-sT_{\mathrm{on}}}}{R_cC_f+\frac{T_{\mathrm{off}}}{2}+\frac{T_s}{e^{sT_s}-1}} \\ &= \frac{1}{T_{\mathrm{on}}}\left(\frac{R_cC_f}{s}+\frac{1}{s^2}\right)\frac{1-e^{-sT_{\mathrm{on}}}}{R_cC_f-\frac{T_{\mathrm{on}}}{2}+\frac{\pi}{j\omega_s}\cot\left(\pi\frac{s}{j\omega_s}\right)}. \end{aligned} \tag{A2}$$

References

[1] R. Redl and J. Sun, "Ripple-based control of switching regulators—An overview," *IEEE Trans. Power Electron.*, vol. 24, no. 12, pp. 2669–2680, Dec. 2009.

[2] D. Goder, "Switching regulator," U.S. Patent 5 770 940, Jun. 23, 1998.

[3] B. Cheng, E. Lee, B. Lynch, and T. Robert, "Choosing the right variable frequency buck regulator control strategy," in *Proc. TI Power Supply Des. Seminar*, 2014, pp. 1–15. [Online]. Available: https://www.ti.com/seclit/wp/slup319/slup319.pdf

[4] J. Sun, "Characterization and performance comparison of ripple-based control for voltage regulator modules," *IEEE Trans. Power Electron.*, vol. 21, no. 2, pp. 346–353, Mar. 2006.

[5] B. Wang, D. Chen, C. J. Chen, and S. F. Hsiao, "Stability prediction of integrated-circuit based constant on-time controlled buck converters," *IEEE Trans. Power Electron*, vol. 36, no. 6, pp. 6838–6849, Jun. 2021.

[6] J. Li, "Current-mode control: Modeling and its digital application," Ph.D. dissertation, Dept. Elect. Eng., Virginia Tech., Blacksburg, VA, USA, 2009.

[7] S. Tian, "Equivalent circuit model of high frequency pulse-width- modulation (PWM) and resonant converters," Ph.D. dissertation, Dept. Elect. Eng., Virginia Tech, Blacksburg, VA, USA, 2015.

[8] Y. Yan, "Equivalent circuit model for current mode controls and its extensions," Ph.D. dissertation, Dept. Elect. Eng., Virginia Tech., Blacksburg, VA, USA, 2013.

[9] J. Sun, "Small-signal modeling of variable-frequency pulsewidth modulators," *IEEE Trans. Aerosp. Electron. Syst.*, vol. 38, no. 3, pp. 1104–1108, Jul. 2002.

[10] L. B. W. Jolley, M. A. (CANTAB.), and M. I. E. E, *Summation of Series*, 2nd ed. Toronto, ON, Canada: Dover, 2014, pp. 102–152.

[11] D. J. Packard, "Discrete modeling and analysis of switching regulators," Ph.D. dissertation, California Inst. Technol., Pasadena, CA, USA, 1976.

[12] D. M. van de Sype, K. D. Gusseme, A. P. van den Bossche, and J. Melkebeek, "Small-signal z-domain analysis of digitally controlled converters," in *Proc. IEEE 35th Annu. Power Electron. Spec. Conf.*, 2004, pp. 4299–4305.

[13] D. Maksimovic and R. Zane, "Small-signal discrete-time modeling of digitally controlled PWM converters," *IEEE Trans. Power Electron.*, vol. 22, no. 6, pp. 2552–2556, Nov. 2007.
[14] L. Corradini, D. Maksimovic, P. Mattavelli, and R. Zane, *Digital Control of High-Frequency Switched-Mode Power Converters*. New York, NY, USA: Wiley, 2015.
[15] F. D. Tan and R. D. Middlebrook, "A unified model for current- programmed converters," *IEEE Trans. Power Electron.*, vol. 10, no. 4, pp. 397–408, Jul. 1995.

Na Yan received the B.S. degree in electrical engineering with the Northeastern University, Shenyang, China, in 2014. She is currently working toward the Ph.D. degree in electrical engineering with the Nanjing University of Aeronautics and Astronautics (NUAA), Nanjing, China.

Her research interests include point-of-load power converters, dynamic modeling, and control of power electronics.

Xinbo Ruan (Fellow, IEEE) received the B.S. and Ph.D. degrees in electrical engineering from the Nanjing University of Aeronautics and Astronautics (NUAA), Nanjing, China, in 1991 and 1996, respectively.

In 1996, he was with the Faculty of Electrical Engineering Teaching and Research Division, NUAA, where he became a Professor with the College of Automation Engineering in 2002 and has been engaged in teaching and research in the field of power electronics. From August 2007 to October 2007, he was a Research Fellow with the Department of Electronic and Information Engineering, Hong Kong Polytechnic University, Hong Kong. From March 2008 to September 2011, he was also with the School of Electrical and Electronic Engineering, Huazhong University of Science and Technology, Wuhan, China. He has authored or coauthored 11 books and more than 300 technical papers published in journals and conferences. His main research interests include soft-switching dc–dc converters, soft-switching inverters, power factor correction converters, modeling the converters, power electronics system integration, and renewable energy generation system.

Dr. Ruan has been a member of the Technical Committee on Renewable Energy Systems within the IEEE Industrial Electronics Society since 2008. He is currently an Associate Editor for the IEEE TRANSACTIONS ON INDUSTRIAL ELECTRONICS, IEEE TRANSACTIONS ON POWER ELECTRONICS, *IEEE Journal of Emerging and Selected Topics on Power Electronics*, IEEE TRANSACTIONS ON CIRCUITS AND SYSTEMS–II, and the *Open Journal of the IEEE Industrial Electronics Society*. From 2005 to 2013, and since 2017 again, he has been a Vice President of the China Power Supply Society. He was the recipient of the Delta Scholarship by the Delta Environment and Education Fund, in 2003, and the Special Appointed Professor of the Chang Jiang Scholars Program by the Ministry of Education, China, in 2007.

Xin Li (Member, IEEE) received the B.S. and Ph.D. degrees in electrical engineering and automation from Nanjing University of Aeronautics and Astronautics, Nanjing, China, in 2012 and 2018, respectively.

In 2019, he was a Research Engineer with Huawei Technologies Co., Ltd., Shanghai, China. Since 2020, he has been a Research Fellow with Nanyang Technological University, Singapore. His current research interests include modeling, control and design of PWM converter, resonant converter, and wireless power transfer system.